nature COMMUNICATIONS

ARTICLE

Received 7 Apr 2016 | Accepted 31 Aug 2016 | Published 11 Oct 2016

DOI: 10.1038/ncomms13069 OPEN

Spin-torque generator engineered by natural oxidation of Cu

Hongyu An[1,*], Yuito Kageyama[1,*], Yusuke Kanno[1], Nagisa Enishi[1] & Kazuya Ando[1,2]

The spin Hall effect is a spin–orbit coupling phenomenon, which enables electric generation and detection of spin currents. This relativistic effect provides a way for realizing efficient spintronic devices based on electric manipulation of magnetization through spin torque. However, it has been believed that heavy metals are indispensable for the spin–torque generation. Here we show that the spin Hall effect in Cu, a light metal with weak spin–orbit coupling, is significantly enhanced through natural oxidation. We demonstrate that the spin–torque generation efficiency of a Cu/$Ni_{81}Fe_{19}$ bilayer is enhanced by over two orders of magnitude by tuning the surface oxidation, reaching the efficiency of Pt/ferromagnetic metal bilayers. This finding illustrates a crucial role of oxidation in the spin Hall effect, opening a route for engineering the spin–torque generator by oxygen control and manipulating magnetization without using heavy metals.

[1] Department of Applied Physics and Physico-Informatics, Keio University, 3-14-1 Hiyoshi, Yokohama 223-8522, Japan. [2] PRESTO, Japan Science and Technology Agency, Kawaguchi, Saitama 332-0012, Japan. * These authors contributed equally to this work. Correspondence and requests for materials should be addressed to K.A. (email: ando@appi.keio.ac.jp).

Interconversion between spin and charge currents is an essential building block of spin-based technologies[1,2]. A promising route for the interconversion is the direct use of spin–orbit interaction, which couples the spin of an electron to its momentum[3–11]. In the presence of the spin–orbit interaction, a non-zero spin current is generated in a direction perpendicular to an applied charge current, which is known as the direct spin Hall effect (DSHE)[12–19]. The spin–orbit interaction also causes the inverse process of the DSHE, a process that converts a spin current into a charge current: the inverse SHE[20–32]. The SHEs enable electric generation and detection of spin currents, offering new concepts of spintronic devices: spin Hall devices[33], such as SHE transistors[34], spin photodetectors[35,36], spin thermoelectric converters[37,38] and spin Hall magnetic memories[18].

A key challenge for the development of such spin Hall devices is to achieve efficient conversion between spin and charge currents. However, to realize efficient spin-charge conversion, it has been believed that heavy metals with strong spin–orbit interaction are indispensable. This largely limits the selection of materials for the practical application of the spin Hall devices. Typically, a noble metal, Pt with around 10% conversion efficiency between spin and charge currents, has been used in most previous studies as a detector of spin currents or a generator of spin torque for magnetization manipulation. On the other hand, light metals have been confirmed to exhibit negligible SHEs. For instance, the conversion efficiency of Cu, a representative light metal with weak spin–orbit coupling, has been quantified to be two orders of magnitude smaller than that of Pt[9,39], which has precluded using this low-cost light metal as a spin-charge converter. Thus, whether the SHEs can be enhanced in light metals is an important fundamental and practical question to push forward the application of the spin Hall devices with a large selection of materials.

In this study, we demonstrate that Cu becomes an efficient spin–torque generator through natural oxidation. This is evidenced by measuring spin–torque ferromagnetic resonance (ST-FMR) for Cu/$Ni_{81}Fe_{19}$ bilayers. The ST-FMR results show that the spin–torque generation efficiency from the Cu layer can be tuned by controlling the surface oxidization. We found that the maximum spin–torque generation efficiency in the naturally oxidized Cu/$Ni_{81}Fe_{19}$ bilayer is comparable to that in Pt/ferromagnetic metal bilayers. Our results also indicate that the observed spin–orbit torque in the naturally oxidized Cu/$Ni_{81}Fe_{19}$ bilayer cannot be attributed to interfacial spin–orbit coupling or the Rashba spin splitting. Thus, the efficient spin–torque generation revealed in the Cu/$Ni_{81}Fe_{19}$ bilayer demonstrates significant enhancement of the DSHE through the natural oxidation of Cu. These results provide a way for engineering the spin–torque generator driven by the DSHE through oxidation control.

Results

Spin–torque FMR. We use the ST-FMR technique to determine the generation efficiency of the spin–orbit torques affected by the natural oxidation of Cu/$Ni_{81}Fe_{19}$ bilayers[13]. In the ST-FMR experiment, a microwave-frequency charge current is applied along the longitudinal direction of the device and an in-plane external magnetic field $\mu_0 H$ is applied with an angle of 45° from the longitudinal direction of the device as shown in Fig. 1a. The radio frequency (RF) current in the Cu layer generates an oscillating transverse spin current through the DSHE and then is injected into the adjacent $Ni_{81}Fe_{19}$ layer. The magnetization of the $Ni_{81}Fe_{19}$ layer is influenced by two torques generated from the RF charge current, an in-plane torque and an out-of-plane torque[13]. When the microwave frequency and the external magnetic field satisfy the FMR condition, the magnetization precession driven by the two torques will result in an oscillation of the resistance due to the anisotropic magnetoresistance in the $Ni_{81}Fe_{19}$ layer. By using a bias tee, a DC voltage signal across the device from the mixing of the RF current and oscillating resistance can be measured simultaneously during the microwave current application.

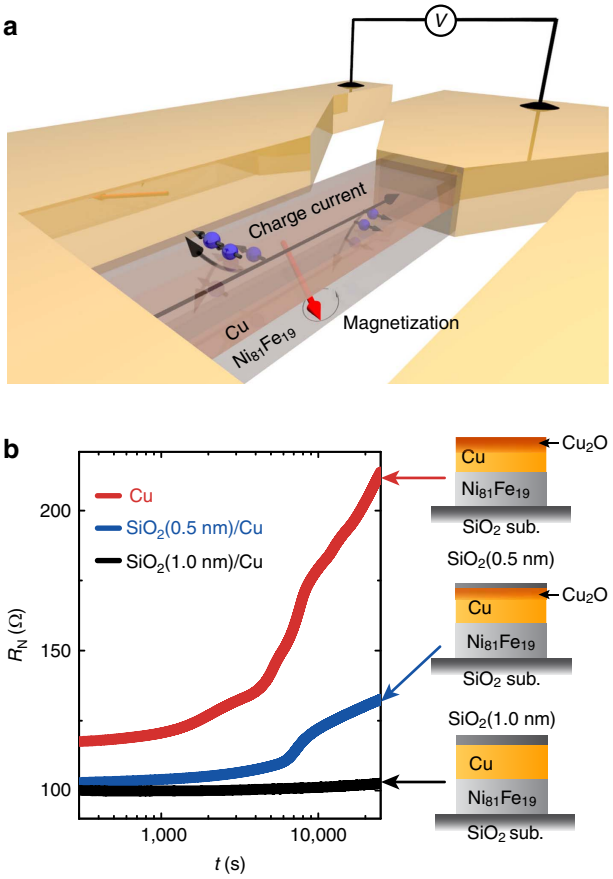

Figure 1 | Device structure. (**a**) Schematic of a Cu/$Ni_{81}Fe_{19}$ bilayer for the ST-FMR measurements. The red arrow represents precessing magnetization in the $Ni_{81}Fe_{19}$ layer. The black arrows indicate the flow of conduction electrons in the Cu layer. An RF charge current was applied along the longitudinal direction of the Cu/$Ni_{81}Fe_{19}$ bilayer. (**b**) The time evolution of the electrical resistance R_N of the Cu layers capped with different thickness SiO_2. The Cu layer was fabricated on a 8 nm-thick $Ni_{81}Fe_{19}$ film and R_N of the Cu layer was extracted from the electrical resistance of the SiO_2/Cu/$Ni_{81}Fe_{19}$ film. The sample size for the resistance measurement was designed as same as that used in the ST-FMR measurements. The time $t = 0$ was defined as the moment when the lift-off procedure was finished for each sample.

The Cu/$Ni_{81}Fe_{19}$ bilayer films used in the ST-FMR measurement were deposited by magnetron sputtering (for details, see Methods). Photolithography and lift-off techniques were used to pattern the films into rectangular strips with 10 μm width and 150 μm length. To tune the natural oxidation level in the Cu layers, the surfaces of the Cu layers were capped by SiO_2 films with different thicknesses using sputtering from a compositional target. This method to control the natural oxidation has been well studied previously[40]. In fact, in the Cu/$Ni_{81}Fe_{19}$ bilayers, the time evolution of the electrical resistance R_N of the Cu layer due to the natural oxidation depends on the thickness of the SiO_2 capping layer as shown in Fig. 1b, indicating that the oxidation level in the Cu layer can be tuned by the thickness of the capping layer as well as the time the bilayer exposed to the laboratory ambient.

Figure 2a shows the ST-FMR spectra of the Cu(10 nm)/$Ni_{81}Fe_{19}$(8 nm) bilayer capped with a 1.0 nm-thick SiO_2 film measured at a frequency of 7.0 GHz. As shown in Fig. 2a, the DC voltage signal V_{mix} significantly changes under the FMR condition. In the ST-FMR measurement, V_{mix} is expressed as[13,41]

$$V_{mix} = S\frac{W^2}{(\mu_0 H - \mu_0 H_{FMR})^2 + W^2} + A\frac{W(\mu_0 H - \mu_0 H_{FMR})}{(\mu_0 H - \mu_0 H_{FMR})^2 + W^2}, \quad (1)$$

where S, A, W and $\mu_0 H_{FMR}$ are the magnitude of the symmetric component, the magnitude of the antisymmetric component, the spectral width and the FMR field, respectively. As shown in Fig. 2a, the experimental results are well reproduced using equation (1) (see the red curve). Based on the fitting result, the symmetric and antisymmetric voltage signals are also plotted separately in the lower part of Fig. 2a. Here, the symmetric part is proportional to the damping-like spin–orbit torque and the antisymmetric part is due to the sum of the Oersted field torque and the field-like spin–orbit torque[42]. Thus, the negligible symmetric voltage shown in Fig. 2a indicates inefficient generation of the damping-like torque in the SiO_2(1 nm)/Cu(10 nm)/$Ni_{81}Fe_{19}$(8 nm) device, consistent with the weak DSHE in Cu, which is protected from surface oxidation.

To directly compare the influence of the oxidation level on the spin–torque generation, we measured the ST-FMR for the Cu/$Ni_{81}Fe_{19}$ films with different thicknesses of the SiO_2 capping layer. Notably, as shown in Fig. 2b, the symmetric component of the voltage signal appears by reducing the thickness of the SiO_2 capping layer from 1.0 to 0.5 nm. Furthermore, the ratio of the symmetric voltage to the antisymmetric voltage further increases in the Cu/$Ni_{81}Fe_{19}$ film, where the capping SiO_2 layer is absent, as shown in Fig. 2c. These results demonstrate that the spin–torque generation efficiency is enhanced by the natural oxidation in the Cu/$Ni_{81}Fe_{19}$ bilayer, because the oxidation level of the Cu layer is tuned by the thickness of the SiO_2 layer. We also studied the voltage generation for a single-layer $Ni_{81}Fe_{19}$(8 nm) film capped with a 4 nm-thick SiO_2 as shown in the inset of Fig. 2a. The $Ni_{81}Fe_{19}$ film gives a purely antisymmetric signal, which arises from an Oersted field induced by the non-uniform current flow at the ends of the $Ni_{81}Fe_{19}$ due to the electrode contacts[13,43]. The lack of field-symmetric components in the resonance curve supports that the symmetric voltage signals observed in the naturally oxidized Cu/$Ni_{81}Fe_{19}$ bilayers arise from the oxidized Cu layer.

To quantitatively investigate the influence of the oxidation in the Cu layer on the spin–torque generation efficiency, we have systematically measured the ST-FMR spectra by changing the current frequency from 4 to 10 GHz as shown in Fig. 3a–c. We have confirmed that the symmetric component of the observed voltage changes the sign by reversing the magnetic field direction (see the inset to Fig. 3c). This sign reversal is consistent with the prediction of the spin–torque-driven FMR[13]. By fitting the measured voltage using equation (1) and using[13,41]

$$\xi_{FMR} = \frac{S}{A}\frac{e\mu_0 M_s d_F d_N}{\hbar}\sqrt{1 + \frac{\mu_0 M_s}{\mu_0 H_{FMR}}}, \quad (2)$$

we determined the FMR spin–torque efficiency ξ_{FMR} for the Cu/$Ni_{81}Fe_{19}$ bilayers as shown in Fig. 3d–f, where d_F and d_N are the thicknesses of the $Ni_{81}Fe_{19}$ layer and the Cu layer, respectively. Here, the saturation magnetization M_s was obtained from the microwave frequency f dependence of the FMR field $\mu_0 H_{FMR}$ using the Kittel formula: $(2\pi f/\gamma) = \sqrt{\mu_0 H_{FMR}(\mu_0 H_{FMR} + \mu_0 M_s)}$, where γ is the gyromagnetic ratio.

Figure 3 demonstrates significant enhancement of ξ_{FMR}, or the spin–torque generation efficiency, by the natural oxidation of the Cu layers. By averaging all the measured values of ξ_{FMR} at different frequencies, we obtain $\xi_{FMR} = 0.13 \pm 0.0079$ for the Cu/$N_{81}Fe_{19}$ bilayer without the SiO_2 capping layer (see Fig. 3f). This large value is more than two orders of magnitude larger than that for the SiO_2(1 nm)/Cu/$N_{81}Fe_{19}$ device ($\xi_{FMR} = 0.00087 \pm 0.00032$), where the Cu layer is protected from the natural oxidation (see Fig. 3a,d). The experimentally measured FMR

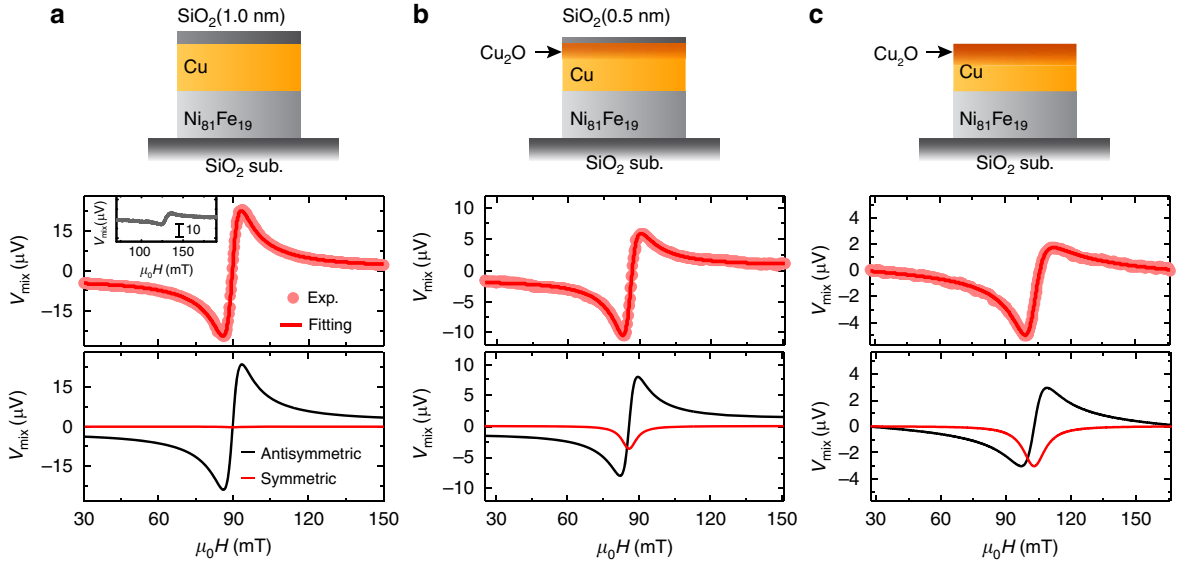

Figure 2 | ST-FMR spectra of the Cu/$Ni_{81}Fe_{19}$ bilayers. The magnetic field $\mu_0 H$ dependence of the DC voltage V_{mix} at 7 GHz for the (**a**) SiO_2(1 nm)/Cu(10 nm)/$Ni_{81}Fe_{19}$(8 nm), (**b**) SiO_2(0.5 nm)/Cu(10 nm)/$Ni_{81}Fe_{19}$(8 nm) and (**c**) Cu(10 nm)/$Ni_{81}Fe_{19}$(8 nm) devices. The schematic illustrations of the natural oxidation manipulation in the Cu layers by changing the thickness of the SiO_2 capping layer are also shown. The RF power of 24.7 dBm was applied for all the measurements. The solid circles are the experimental data and the solid curves are the fitting result using equation (1). The inset in **a** shows the V_{mix} spectrum for the SiO_2(4 nm)/$Ni_{81}Fe_{19}$(8 nm) film at 7 GHz. The symmetric and antisymmetric components of the fitting results are plotted correspondingly.

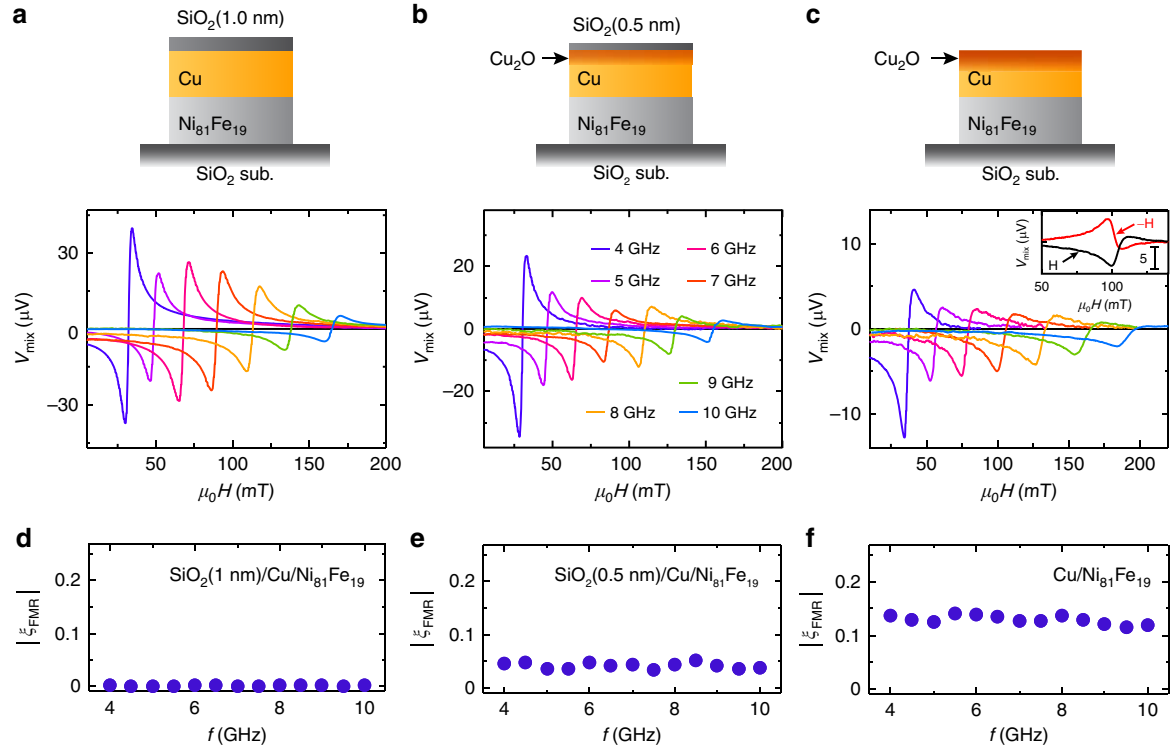

Figure 3 | Spin-torque generation efficiency. The ST-FMR spectra for the (**a**) SiO_2(1 nm)/Cu(10 nm)/$Ni_{81}Fe_{19}$(8 nm), (**b**) SiO_2(0.5 nm)/Cu(10 nm)/$Ni_{81}Fe_{19}$(8 nm) and (**c**) Cu(10 nm)/$Ni_{81}Fe_{19}$(8 nm) devices for different RF current frequencies from 4 to 10 GHz. The inset in **c** shows the ST-FMR spectra at 7 GHz for both positive H and negative H magnetic fields. The FMR spin-torque efficiency ξ_{FMR} for the (**d**) SiO_2(1 nm)/Cu(10 nm)/$Ni_{81}Fe_{19}$(8 nm), (**e**) SiO_2(0.5 nm)/Cu(10 nm)/$Ni_{81}Fe_{19}$(8 nm) and (**f**) Cu(10 nm)/$Ni_{81}Fe_{19}$(8 nm) devices calculated using equation (2).

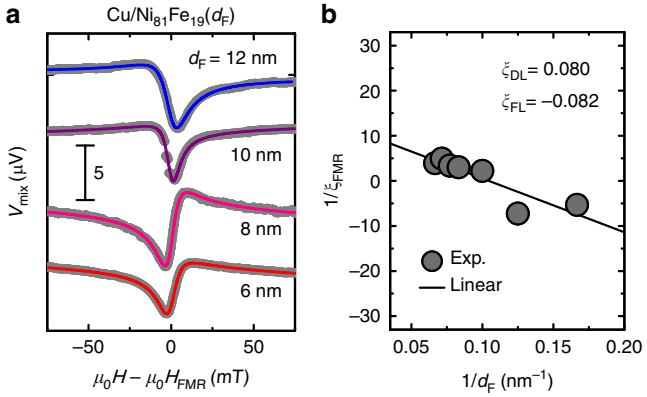

Figure 4 | Thickness dependence of ST-FMR. (**a**) The ST-FMR spectra for the naturally oxidized Cu(10 nm)/$Ni_{81}Fe_{19}$(d_F) bilayers at 7 GHz. d_F is the thickness of the $Ni_{81}Fe_{19}$ layer. (**b**) The inverse of the FMR spin-torque efficiency $1/\xi_{FMR}$ as a function of $1/d_F$ for the naturally oxidized Cu/$Ni_{81}Fe_{19}$ bilayer. The solid circles are the experimental data and the solid line is the linear fit to the data.

spin–torque efficiency ξ_{FMR} is related to the damping-like ξ_{DL} and field-like ξ_{FL} spin–torque efficiencies as[42]

$$\frac{1}{\xi_{FMR}} = \frac{1}{\xi_{DL}}\left(1 + \frac{\hbar}{e}\frac{\xi_{FL}}{\mu_0 M_s d_F d_N}\right). \quad (3)$$

To determine ξ_{DL} and ξ_{FL}, we measured $Ni_{81}Fe_{19}$ layer thickness d_F dependence of the ST-FMR spectra for the naturally oxidized Cu/$Ni_{81}Fe_{19}$ bilayer (see Fig. 4a,b). Figure 4a shows that the sign of the antisymmetric component of V_{mix} changes by changing the thickness of the $Ni_{81}Fe_{19}$ layer, indicating the presence of both the field-like torque and the Oersted torque with opposite signs[42]. From the $1/d_F$ dependence of $1/\xi_{FMR}$ shown in Fig. 4b with equation (3), we obtain $\xi_{DL} = 0.080$ and $\xi_{FL} = -0.082$ for the naturally oxidized Cu/$Ni_{81}Fe_{19}$ bilayer. The positive sign for ξ_{DL} corresponds to the same sign of the damping-like torque as for Pt and the minus sign for ξ_{FL} indicates that the field-like effective field is opposite to the Oersted field[44]. The generation efficiency of the damping-like torque $\xi_{DL} = 0.080$ of the naturally oxidized Cu/$Ni_{81}Fe_{19}$ bilayer is comparable to that of Pt/ferromagnetic metal bilayers (see also Supplementary Fig. 1 and Supplementary Note 1)[42].

Discussion

Our experimental finding is that the spin–torque generation efficiency of the Cu/$Ni_{81}Fe_{19}$ bilayer is significantly enhanced by the natural oxidation; the spin–torque generation efficiency of the naturally oxidized Cu/$Ni_{81}Fe_{19}$ bilayer is comparable to that of Pt/ferromagnetic metal bilayers. There are two possible scenarios of the efficient spin–torque generation from the naturally oxidized Cu: the spin–torque generation by the bulk SHE or the interfacial Rashba effect.

The Rashba effect is unlikely to be the origin of the spin–torque observed in the Cu/$Ni_{81}Fe_{19}$ bilayer. As the Rashba spin splitting arises from electronic discontinuities at interfaces between two distinct materials, the Rashba effect in the naturally oxidized Cu/$Ni_{81}Fe_{19}$ bilayer can be induced at two interfaces: the Cu/$Ni_{81}Fe_{19}$ and oxidized Cu/Cu interfaces. First, the spin–torque due to the Rashba effect at the Cu/$Ni_{81}Fe_{19}$ interface is negligible in the naturally oxidized Cu/$Ni_{81}Fe_{19}$ bilayer. In the naturally oxidized Cu/$Ni_{81}Fe_{19}$ bilayer, the Cu/$Ni_{81}Fe_{19}$ interface is not affected by the natural oxidation, as the surface oxidation in the Cu/$Ni_{81}Fe_{19}$ bilayer used for the ST-FMR measurement can be as much as 4 nm into the bulk and the interface is barely

affected by the oxidation (see also Methods)[45]. Therefore, the Rashba spin–torque generated at the Cu/$Ni_{81}Fe_{19}$ interface in the naturally oxidized Cu/$Ni_{81}Fe_{19}$ bilayer can be estimated from the ST-FMR result for the SiO_2-covered Cu/$Ni_{81}Fe_{19}$ bilayer. As shown in Fig. 3d, the spin–torque in the SiO_2(1 nm)/Cu/$Ni_{81}Fe_{19}$ device is negligible, demonstrating negligible Rashba spin torque at the Cu/$Ni_{81}Fe_{19}$ interface in the naturally oxidized Cu/$Ni_{81}Fe_{19}$ bilayer. Second, the Rashba effect that can be induced at the oxidized Cu/Cu interface also does not produce sizable spin–torque enough to explain the experimental observation. The Rashba effect, characterized by the Rashba coefficient α_R, creates a three-dimensional spin current j_s^R from an interfacial 2D charge current j_c^I as ref. 46

$$j_s^R = \frac{m^* \alpha_R}{\hbar \tau_s \varepsilon_F} j_c^I, \qquad (4)$$

where τ_s is the effective relaxation time, m^* is the effective electron mass and ε_F is the Fermi energy. In the presence of the Rashba spin splitting at the oxidized Cu/Cu interface, the spin current j_s^R generated at the oxidized Cu/Cu interface diffuses through the Cu layer, which can give rise to a spin–torque on the magnetization in the $Ni_{81}Fe_{19}$ layer. To estimate the lowest value of the Rashba coefficient α_R required to reproduce the experimental result $\xi_{DL} = j_s^F/j_c = 0.080$, we neglect the spin relaxation and spin memory loss in the naturally oxidized Cu/$Ni_{81}Fe_{19}$ bilayer: $j_s^F = j_s^R$, where j_s^F is the spin current density injected into the $Ni_{81}Fe_{19}$ layer and j_c is the charge current density in the naturally oxidized Cu layer. Using $j_c^I = tj_c$, where $t = 0.5$ nm is the interface thickness[47,48], and equation (4) with $m^* = 9.20 \times 10^{-31}$ kg, $\tau_s = 0.5 \times 10^{-14}$ s and $\varepsilon_F = 7.0$ eV[47,49], we obtain the Rashba coefficient that reproduces the observed $\xi_{DL} = 0.080$ as $\alpha_R = 6.5$ eVÅ. This value, the lower bound of α_R, is much larger than the largest value of the Rashba coefficient observed in metallic systems so far[46]. Therefore, this result indicates that the Rashba effect at the oxidized Cu/Cu interface is irrelevant to the efficient spin–torque generation in the naturally oxidized Cu/$Ni_{81}Fe_{19}$ bilayer. Further evidence of the negligible spin–torque due to the Rashba effect at the oxidized Cu/Cu interface is obtained by measuring the ST-FMR for a Cu_2O/Cu/$Ni_{81}Fe_{19}$ trilayer, where the surface of the Cu layer is capped by Cu_2O. The Cu_2O layer was deposited by applying oxygen with a 3% flow ratio into argon gas during the sputtering (for details, see Methods). After the Cu_2O deposition, a SiO_2 layer was capped on the film to prevent further oxidation (see Fig. 5a). Although both Cu_2O/Cu/$Ni_{81}Fe_{19}$ trilayer and naturally oxidized Cu/$Ni_{81}Fe_{19}$ bilayer have the oxidized Cu/Cu interface, we found that the spin–torque generation efficiency in the Cu_2O/Cu/$Ni_{81}Fe_{19}$ trilayer is more than an order of magnitude smaller than that in the naturally oxidized Cu/$Ni_{81}Fe_{19}$ bilayer as shown in Fig. 5b. This result supports that the diffusive spin current generated by the Rashba effect at the oxidized Cu/Cu interface is not responsible for the efficient spin–torque generation in the naturally oxidized Cu/$Ni_{81}Fe_{19}$ bilayer. This result also demonstrates a negligible non-local Rashba–Edelstein field, where the spin accumulation generated at the Rashba interface exchange couples to the magnetization in the $Ni_{81}Fe_{19}$ layer[50]. We also note that in the naturally oxidized Cu/$Ni_{81}Fe_{19}$ bilayer, electrons in the Cu layer reflected from the oxidized Cu/Cu interface can become spin-polarized due to the spin–orbit scattering and then enter the $Ni_{81}Fe_{19}$ layer with their spin being non-collinear to the magnetization[51]. This process can also generate the damping-like torque. However, the negligible symmetric voltage in the ST-FMR spectrum for the Cu_2O/Cu/$Ni_{81}Fe_{19}$ trilayer indicates that the spin torque due to the spin–orbit scattering at the oxidized Cu/Cu interface is negligible. Thus, the efficient spin–torque generation in the naturally oxidized Cu/$Ni_{81}Fe_{19}$ bilayer cannot be attributed to the spin–orbit scattering, as well as the Rashba effect at the oxidized Cu/Cu interface.

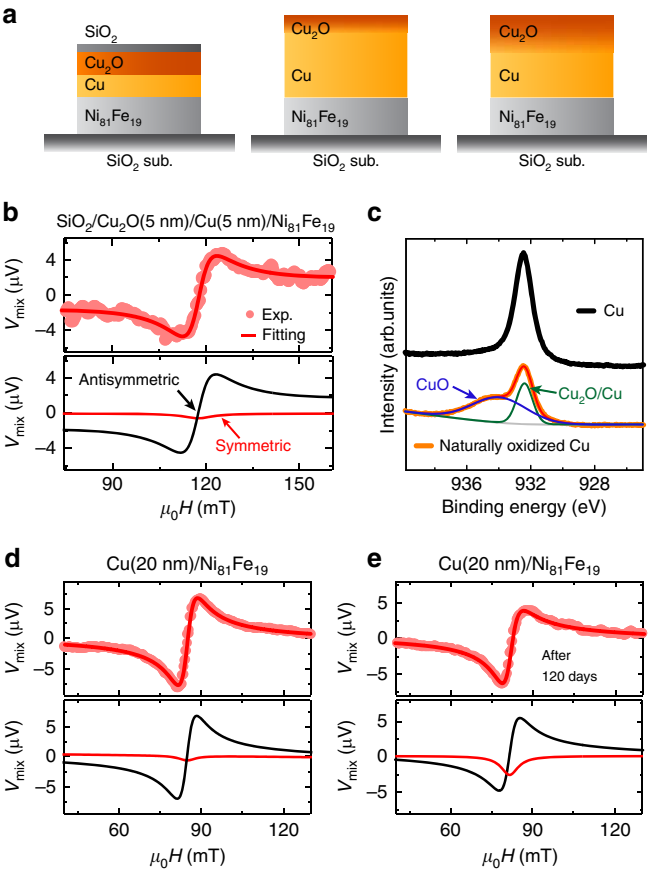

Figure 5 | ST-FMR in different systems and oxidation characterization. (**a**) Schematic illustrations for the SiO_2/Cu_2O(5 nm)/Cu(5 nm)/$Ni_{81}Fe_{19}$, Cu(20 nm)/$Ni_{81}Fe_{19}$ and Cu(20 nm)/$Ni_{81}Fe_{19}$(120 days after the fabrication) devices, respectively. (**b**) The measured and fitted ST-FMR spectra of the SiO_2/Cu_2O(5 nm)/Cu(5 nm)/$Ni_{81}Fe_{19}$(8 nm) film. (**c**) Comparison of the X-ray photoelectron spectra for Cu and naturally oxidized Cu films with thickness of 10 nm. (**d**) The measured and fitted ST-FMR spectra of the Cu(20 nm)/$Ni_{81}Fe_{19}$(8 nm) film at 7 GHz. (**e**) The measured and fitted ST-FMR spectra of the Cu(20 nm)/$Ni_{81}Fe_{19}$(8 nm) film at 7 GHz, where the device was exposed to the laboratory ambient for 120 days after the fabrication.

The above result shows that the efficient spin–torque generation in the naturally oxidized Cu/$Ni_{81}Fe_{19}$ bilayer arises from significant enhancement of the DSHE in the Cu layer through the natural oxidation. Although the exact mechanism responsible for the enhancement is not understood in details, the dominant contribution to the DSHE in the naturally oxidized Cu layer can be attributed to spin-dependent scatterings in the interior of the Cu layer rather than the surface scatterings. The surface scattering strongly affects the spin-dependent transport in Cu because of the long mean free path of the conduction electrons. In fact, the spin relaxation length of Cu is known to be strongly dependent on the thickness[52]. For the SHEs, an important role of the surface scattering has been reported for Au[53]. However, the critical difference in the spin–torque generation efficiency between the Cu_2O/Cu/$Ni_{81}Fe_{19}$ trilayer and naturally oxidized Cu/$Ni_{81}Fe_{19}$ bilayer indicates that the difference in the surface scattering between the oxidized Cu/Cu and SiO_2/Cu interfaces is not the main source of the enhancement of the DSHE induced by the surface oxidation.

In the naturally oxidized Cu, an applied charge current flows in a partially oxidized Cu layer and in the non-oxidized Cu layer. The natural oxidation process creates a duplex-type oxidized structure, $CuO/Cu_2O/Cu$, of an insulating CuO layer at the surface and an inner semiconducting Cu_2O layer[54]. In fact, as shown in Fig. 5c, the CuO peak can be clearly observed after natural oxidation of a Cu film in the X-ray photoelectron spectra. It has been confirmed that the oxygen concentration gradually decreases from the CuO/Cu_2O interface to the interior of the Cu layer[55]; thus, precisely, the Cu_2O layer is a mixture of Cu_2O and non-oxidized Cu. With the surface- or interface-dominated Rashba and SHEs ruled out as mechanisms behind the efficient spin–torque generation in the naturally oxidized $Cu/Ni_{81}Fe_{19}$ bilayer, the only possible mechanism that agrees with the observed damping-like spin–torque is the DSHE in the mixed region of the Cu_2O and non-oxidized Cu layer. Although detailed calculations are necessary to address the mechanism of the giant DSHE in the mixed region, we found that the spin–torque generation efficiency depends on the thickness of the Cu layer; the symmetric component of V_{mix} is negligible in a thicker naturally oxidized Cu(20 nm)/$Ni_{81}Fe_{19}$ bilayer as shown in Fig. 5d. We also found that by further exposing the Cu(20 nm)/$Ni_{81}Fe_{19}$ bilayer to the laboratory ambient, the ratio of the symmetric voltage to the antisymmetric voltage increases as shown in Fig. 5e. For the ST-FMR measurement shown in Fig. 5e, the Cu(20 nm)/$Ni_{81}Fe_{19}$ bilayer was exposed to the laboratory ambient for 120 days after the fabrication, which results in the effective thickness of the oxidized layer of around 6 nm[56]. From this result, we obtained $\xi_{FMR}=0.053$, which is clearly enhanced from $\xi_{FMR}=0.011$ obtained from the result shown in Fig. 5d, supporting that the natural oxidation is responsible for the spin–torque generation in the $Cu/Ni_{81}Fe_{19}$ bilayers. These results are consistent with the DSHE in the intermediate Cu_2O layer, as in the thicker Cu film only a small amount of the applied charge current flows in the highly resistive layer of the mixture of Cu_2O and non-oxidized Cu, and most of the charge current flows in the non-oxidized Cu layer with the negligible DSHE.

To further clarify the role of the natural oxidation in the spin–torque generation, we measured the ST-FMR spectra for $Ni_{81}Fe_{19}$(8 nm)/CuO_x(15.9 nm) bilayers, where the Cu layer was homogeneously oxidized using the reactive RF magnetron sputtering with the mixture of argon and oxygen gas. For the sputtering, the amount of oxygen gas flow Q in the reactive mixture was varied between 0 and 3%. To avoid the oxidation of the $Ni_{81}Fe_{19}$ layer, the CuO_x layer was first sputtered on a SiO_2 substrate and then the $Ni_{81}Fe_{19}$ layer was sputtered on the CuO_x layer. The surface of the $Ni_{81}Fe_{19}$ layer was capped with a 4 nm-thick SiO_2 film. Figure 6a shows the ST-FMR spectra for the $SiO_2/Ni_{81}Fe_{19}/CuO_x$ devices fabricated with different amount of the oxygen gas flow Q. Using this result, we plotted the FMR spin–torque efficiency ξ_{FMR} for the $SiO_2/Ni_{81}Fe_{19}/CuO_x$ as a function of Q in Fig. 6b. This result indicates that a damping-like torque appears in the $SiO_2/Ni_{81}Fe_{19}/CuO_x$ with increasing the homogeneous oxidation level of the Cu layer. Therefore, the spin–orbit torque can be generated not only from the inhomogeneously-oxidized Cu (naturally oxidized Cu) but also from the homogeneously oxidized Cu.

In Fig. 6c, we show ξ_{FMR} as a function of electrical resistivity ρ_N of the CuO_x layer. This result indicates that the FMR spin–torque efficiency does not scale with the electrical resistivity. As shown in Fig. 6d, the electrical resistivity of the Cu layer increases with increasing the oxygen flow Q during the sputtering due to the formation of Cu_2O. Figure 6d also shows that the further increase of Q results in the lowering of the electrical resistivity. The lowering of the resistivity has been explained as resulting from the excess oxygen doping, which effectively produces more copper ion vacancies in the p-type semiconductor Cu_2O (ref. 57). Thus, these results demonstrate that the FMR spin–torque efficiency in the $SiO_2/Ni_{81}Fe_{19}/CuO_x$ is dominated by the oxidation level of the Cu layer rather than the electrical resistivity of the CuO_x layer.

In contrast to the spin–torque generation in the naturally oxidized $Cu/Ni_{81}Fe_{19}$ bilayer, the origin of the spin–torque observed in the $SiO_2/Ni_{81}Fe_{19}/CuO_x$ bilayer cannot be attributed

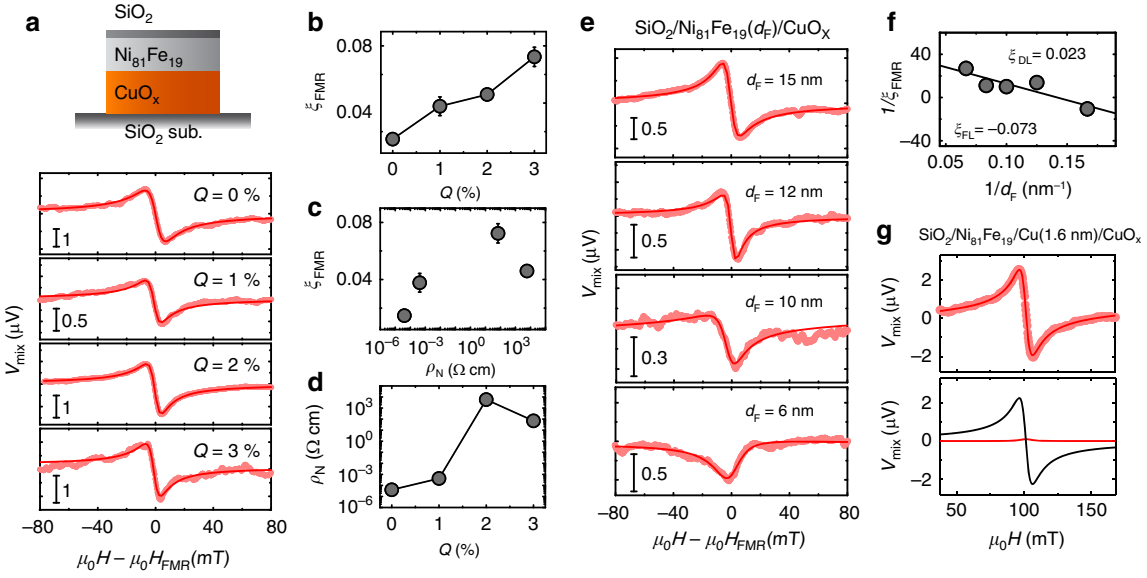

Figure 6 | ST-FMR spectra of the $Ni_{81}Fe_{19}/CuO_x$ bilayers. (**a**) The ST-FMR spectra for the SiO_2(4 nm)/$Ni_{81}Fe_{19}$(8 nm)/CuO_x(15.9 nm) films with different Q at 7 GHz. (**b**) The Q dependence of ξ_{FMR} for the $SiO_2/Ni_{81}Fe_{19}/CuO_x$. The error bars are defined as s.e.m. (**c**) ξ_{FMR} for the $SiO_2/Ni_{81}Fe_{19}/CuO_x$ device as a function of the electrical resistivity ρ_N of the CuO_x layer. (**d**) The Q dependence of the electrical resistivity ρ_N of the CuO_x layer. (**e**) The ST-FMR spectra for the $SiO_2/Ni_{81}Fe_{19}/CuO_x$ with $Q=3\%$ for different d_F at 7 GHz, where d_F is the thickness of the $Ni_{81}Fe_{19}$ layer. (**f**) The inverse of the FMR spin–torque efficiency $1/\xi_{FMR}$ as a function of $1/d_F$ for the $SiO_2/Ni_{81}Fe_{19}/CuO_x$. The solid circles are the experimental data and the solid line is the linear fit to the data. (**g**) The measured and fitted ST-FMR spectra of the SiO_2(4 nm)/$Ni_{81}Fe_{19}$(8 nm)/Cu(1.6 nm)/CuO_x(14.3 nm) film at 7 GHz.

to the DSHE in the homogeneously oxidized Cu layer. Here, it is noteworthy that at $Q = 3\%$ the electrical resistance of the CuO_x layer exceeds $3 \times 10^8\,\Omega$, which is six orders of magnitude larger than that of the $Ni_{81}Fe_{19}$ layer. Thus, most of the applied charge current flows in the $Ni_{81}Fe_{19}$ layer and only a fraction of the charge current flows in the CuO_x layer. The negligible charge current in the CuO_x layer cannot generate the sizable symmetric voltage or the damping-like torque, through the DSHE in the $SiO_2/Ni_{81}Fe_{19}/CuO_x$ devices. To determine the damping-like ξ_{DL} and field-like ξ_{FL} spin–torque efficiencies in the $SiO_2/Ni_{81}Fe_{19}/CuO_x$ structure with $Q = 3\%$, we measured the ST-FMR spectra for different $Ni_{81}Fe_{19}$ layer thickness d_F as shown in Fig. 6e. In Fig. 6f, we show $1/\xi_{FMR}$ as a function of $1/d_F$. From this result with equation (3), we obtain $\xi_{DL} = 0.023$ and $\xi_{FL} = -0.073$ for the $SiO_2/Ni_{81}Fe_{19}/CuO_x$ with $Q = 3\%$. The efficient generation of the field-like torque, rather than the damping-like torque, supports that the spin–torque arises not from the DSHE in the CuO_x layer but from the Rashba effect[48].

The difference in the naturally oxidized $Cu/Ni_{81}Fe_{19}$ bilayer and the $Ni_{81}Fe_{19}/CuO_x$ bilayer is the interface oxidation and the homogeneity of the oxidation level in the Cu layer. In the naturally oxidized $Cu/Ni_{81}Fe_{19}$ bilayer, the oxidation level of the Cu layer decreases exponentially from the surface and the $Cu/Ni_{81}Fe_{19}$ interface is not affected by the natural oxidation. In contrast, in the $Ni_{81}Fe_{19}/CuO_x$ bilayer, the $Ni_{81}Fe_{19}$ layer is in direct contact with the oxidized Cu layer. This difference of the interface gives rise to the different mechanisms responsible for the spin–torque generation. In Fig. 6g, we show the ST-FMR spectrum for a $SiO_2/Ni_{81}Fe_{19}(8\,nm)/Cu(1.6\,nm)/CuO_x(14.3\,nm)$ device with $Q = 3\%$. This result demonstrates that the symmetric component of V_{mix}, or the damping-like torque, becomes negligible by inserting the very thin Cu layer. From the result shown in Fig. 6g, the FMR spin–torque efficiency for the $SiO_2/Ni_{81}Fe_{19}/Cu(1.6\,nm)/CuO_x$ is determined to be $\xi_{FMR} = 0.009 \pm 0.002$, which is about an order of magnitude smaller than that for the $SiO_2/Ni_{81}Fe_{19}/CuO_x$. This result supports that the direct contact between the $Ni_{81}Fe_{19}$ and CuO_x layers is essential for the spin–torque generation in the $SiO_2/Ni_{81}Fe_{19}/CuO_x$ device (see also Fig. 5b). This is clearly different from the spin–torque generation in the naturally oxidized $Cu/Ni_{81}Fe_{19}$ bilayer, as in the bilayer the sizable damping-like torque is observed, despite the fact that the $Ni_{81}Fe_{19}$ layer and oxidized Cu layer are separated by non-oxidized Cu. Although the DSHE in the interior of the CuO_x layer can be enhanced with the oxidation level as same as the naturally oxidized Cu, our results suggest that the spin–orbit torque generated by the Rashba effect at the $Ni_{81}Fe_{19}/CuO_x$ interface exceeds that generated by the DSHE of the CuO_x layer in the $Ni_{81}Fe_{19}/CuO_x$ bilayer. We also note that the ratio of the symmetric voltage to the antisymmetric voltage is almost independent of the thickness of the inserted Cu layer as shown in Figs 5b and 6g. In these devices, because of the high resistivity of the oxidized Cu layer, most of the applied current flows in the Cu layer. Thus, the effect of electron scatterings at the Cu/CuO_x and $Ni_{81}Fe_{19}/Cu$ interfaces on the spin–torque generation is expected to become significant by decreasing the thickness of the inserted Cu layer. Nevertheless, we found negligible difference in the ST-FMR spectra for the trilayers with different Cu thicknesses. This demonstrates again that the spin–orbit scattering at the oxidized Cu/Cu and $Ni_{81}Fe_{19}/Cu$ interfaces plays a minor role in the spin–torque generation in the naturally oxidized $Cu/Ni_{81}Fe_{19}$ bilayers.

The significant enhancement of the spin–torque demonstrates the crucial role of the natural oxidation in the DSHE. This finding is clearly different from recent observations of the interfacial Rashba spin–orbit torque affected by oxygen incorporation[40,58]. The damping-like spin–torque efficiency ξ_{DL} obtained from the ST-FMR measurements is related to the spin Hall angle θ_{SHE} as $\xi_{DL} = j_s^F/j_c = T_{int}\theta_{SHE}$ when $d_N \gg \lambda_N$, where T_{int} is the interfacial spin transparency and λ_N is the spin-diffusion length of the non-magnetic layer[59]. However, this simple model cannot be applied directly to the present naturally oxidized $Cu/Ni_{81}Fe_{19}$ bilayer, as the spin Hall angle, as well as the charge and spin transport properties in the naturally oxidized Cu film are spatially non-uniform. A detailed theoretical calculation, which takes into account the spatial inhomogeneity of the spin and charge transport, is necessary to provide a detailed physical mechanism responsible for the DSHE in Cu induced by natural oxidation. Therefore, the finding of the spin–torque generation in the naturally oxidized $Cu/Ni_{81}Fe_{19}$ bilayers will serve as a stimulation of in-depth theoretical studies of the spin transport and our results provide an important piece of information for deeper understanding of the spin–orbit physics in solids. Furthermore, the efficient spin–torque generator achieved by the natural oxidation provides a route for developing efficient spintronic devices through oxidation engineering, promising important advances in spintronics and oxide electronics.

Methods

Sample preparation. The films were deposited on thermally oxidized Si substrates by RF magnetron sputtering at room temperature. The base pressure in the chamber before the deposition was better than 1×10^{-6} Pa and the deposition pressure was 0.2 Pa. The $Ni_{81}Fe_{19}$, Cu and SiO_2 films were deposited by applying argon gas with flow rate of 10 s.c.c.m. The Cu layer was sputtered from a 99.99% purity target. For the Cu_2O deposition, oxygen and argon gases were applied with flow rate of 0.3 and 9.7 s.c.c.m., respectively. The film thicknesses were controlled by the deposition time with a pre-calibrated deposition rate. For the fabrication of the devices used in ST-FMR experiment, the substrates were patterned into 10 μm × 150 μm rectangular shape by standard photolithography before deposition and lift-off technique was used to take off the rest part of the films after deposition. The ST-FMR experiments were taken within 5 h for all the devices after the fabrication, except for the notified cases. For the comparison between Cu and naturally oxidized Cu films in the X-ray photoelectron spectroscopy, two Cu blanket films with the thickness of 10 nm were used, where one sample was measured within 1 h after the fabrication and the other one was exposed to the laboratory ambient for 5 days before the measurement. All measurements were conducted at room temperature.

Electric resistance. The time evolution of the electrical resistance R_N of the Cu layer shown in Fig. 1b was measured using the conventional four-probe method for the $Cu/Ni_{81}Fe_{19}$ bilayers with different thickness SiO_2. The resistance of the $Ni_{81}Fe_{19}$ layer was eliminated from the measured resistance of the bilayers. From the change of the resistance R_N of the Cu layer, the effective thickness of the oxidized layer can be estimated as ~4 nm in the 10 nm-thick Cu layer at the time when the ST-FMR was measured. For the estimation, we neglected the gradual change of the oxidation level and the charge-current flow in the oxidized layer for simplicity. This result supports that the $Cu/Ni_{81}Fe_{19}$ interface is not affected by the natural oxidation of the $Cu/Ni_{81}Fe_{19}$ bilayers.

Data availability. The data that support the findings of this study are available from the corresponding author on request.

References

1. Žutić, I., Fabian, J. & Das Sarma, S. Spintronics: fundamentals and applications. *Rev. Mod. Phys.* **76,** 323–410 (2004).
2. Maekawa, S. (ed.) *Concepts in Spin Electronics* (Oxford Univ. Press, 2006).
3. Dyakonov, M. I. & Perel, V. I. Current-induced spin orientation of electrons in semiconductors. *Phys. Lett.* **35A,** 459–460 (1971).
4. Hirsch, J. E. Spin Hall effect. *Phys. Rev. Lett.* **83,** 1834–1837 (1999).
5. Murakami, S., Nagaosa, N. & Zhang, S. C. Dissipationless quantum spin current at room temperature. *Science* **301,** 1348–1351 (2003).
6. Sinova, J. *et al.* Universal intrinsic spin Hall effect. *Phys. Rev. Lett.* **92,** 126603 (2004).
7. Kato, Y. K., Myers, R. C., Gossard, A. C. & Awschalom, D. D. Observation of the spin Hall effect in semiconductors. *Science* **306,** 1910–1913 (2004).
8. Wunderlich, J., Kaestner, B., Sinova, J. & Jungwirth, T. Experimental observation of the spin-Hall effect in a two-dimensional spin-orbit coupled semiconductor system. *Phys. Rev. Lett.* **94,** 047204 (2005).

9. Sinova, J., Valenzuela, S. O., Wunderlich, J., Back, C. H. & Jungwirth, T. Spin Hall effects. *Rev. Mod. Phys.* **87,** 1213–1260 (2015).
10. Hoffmann, A. Spin Hall effects in metals. *IEEE Trans. Magn.* **49,** 5172–5193 (2013).
11. Niimi, Y. & Otani, Y. Reciprocal spin Hall effects in conductors with strong spin-orbit coupling: a review. *Rep. Prog. Phys.* **78,** 124501 (2015).
12. Ando, K. *et al.* Electric manipulation of spin relaxation using the spin Hall effect. *Phys. Rev. Lett.* **101,** 036601 (2008).
13. Liu, L., Moriyama, T., Ralph, D. & Buhrman, R. Spin-torque ferromagnetic resonance induced by the spin Hall effect. *Phys. Rev. Lett.* **106,** 036601 (2011).
14. Tse, W.-K. & Das Sarma, S. Spin Hall effect in doped semiconductor structures. *Phys. Rev. Lett.* **96,** 056601 (2006).
15. Haazen, P. *et al.* Domain wall depinning governed by the spin Hall effect. *Nat. Mater.* **12,** 299–303 (2013).
16. Garlid, E. S., Hu, Q. O., Chan, M. K., Palmstrøm, C. J. & Crowell, P. A. Electrical measurement of the direct spin Hall effect in Fe/$In_xGa_{1-x}As$ heterostructures. *Phys. Rev. Lett.* **105,** 156602 (2010).
17. Zhang, W. *et al.* Spin Hall effects in metallic antiferromagnets. *Phys. Rev. Lett.* **113,** 196602 (2014).
18. Liu, L. *et al.* Spin-torque switching with the giant spin Hall effect of tantalum. *Science* **336,** 555–558 (2012).
19. Bhowmik, D., You, L. & Salahuddin, S. Spin Hall effect clocking of nanomagnetic logic without a magnetic field. *Nat. Nanotechnol.* **9,** 59–63 (2014).
20. Saitoh, E., Ueda, M., Miyajima, H. & Tatara, G. Conversion of spin current into charge current at room temperature: Inverse spin-Hall effect. *Appl. Phys. Lett.* **88,** 182509 (2006).
21. Kimura, T., Otani, Y., Sato, T., Takahashi, S. & Maekawa, S. Room-temperature reversible spin Hall effect. *Phys. Rev. Lett.* **98,** 156601 (2007).
22. Valenzuela, S. O. & Tinkham, M. Direct electronic measurement of the spin Hall effect. *Nature* **442,** 176–179 (2006).
23. Hahn, C. *et al.* Comparative measurements of inverse spin Hall effects and magnetoresistance in YIG/Pt and YIG/Ta. *Phys. Rev. B* **87,** 174417 (2013).
24. Mosendz, O. *et al.* Quantifying spin Hall angles from spin pumping: experiments and theory. *Phys. Rev. Lett.* **104,** 046601 (2010).
25. Weiler, M. *et al.* Experimental test of the spin mixing interface conductivity concept. *Phys. Rev. Lett.* **111,** 176601 (2013).
26. d'Allivy Kelly, O. *et al.* Inverse spin Hall effect in nanometer-thick yttrium iron garnet/Pt system. *Appl. Phys. Lett.* **103,** 082408 (2013).
27. Castel, V., Vlietstra, N., van Wees, B. J. & Youssef, J. B. Frequency and power dependence of spin-current emission by spin pumping in a thin-film YIG/Pt system. *Phys. Rev. B* **86,** 134419 (2012).
28. Sandweg, C. W. *et al.* Spin pumping by parametrically excited exchange magnons. *Phys. Rev. Lett.* **106,** 216601 (2011).
29. Jiao, H. & Bauer, G. E. W. Spin backflow and ac voltage generation by spin pumping and the inverse spin Hall effect. *Phys. Rev. Lett.* **110,** 217602 (2013).
30. Wei, D., Obstbaum, M., Ribow, M., Back, C. & Woltersdorf, G. Spin Hall voltages from a.c. and d.c. spin currents. *Nat. Commun.* **5,** 3768 (2014).
31. Czeschka, F. D. *et al.* Scaling behavior of the spin pumping effect in ferromagnet-platinum bilayers. *Phys. Rev. Lett.* **107,** 046601 (2011).
32. Mendes, J. *et al.* Large inverse spin Hall effect in the antiferromagnetic metal $Ir_{20}Mn_{80}$. *Phys. Rev. B* **89,** 140406 (2014).
33. Jungwirth, T., Wunderlich, J. & Olejnik, K. Spin Hall effect devices. *Nat. Mater.* **11,** 382–390 (2012).
34. Wunderlich, J. *et al.* Spin Hall effect transistor. *Science* **330,** 1801–1804 (2010).
35. Wunderlich, J. *et al.* Spin-injection Hall effect in a planar photovoltaic cell. *Nat. Phys.* **5,** 675–681 (2009).
36. Ando, K. *et al.* Photoinduced inverse spin-Hall effect: conversion of light-polarization information into electric voltage. *Appl. Phys. Lett.* **96,** 082502 (2010).
37. Uchida, K. *et al.* Spin Seebeck insulator. *Nat. Mater.* **9,** 894–897 (2010).
38. Kirihara, A. *et al.* Spin-current-driven thermoelectric coating. *Nat. Mater.* **11,** 686–689 (2012).
39. Wang, H. *et al.* Scaling of spin Hall angle in 3d, 4d, and 5d metals from $Y_3Fe_5O_{12}$/metal spin pumping. *Phys. Rev. Lett.* **112,** 197201 (2014).
40. Qiu, X. *et al.* Spin-orbit-torque engineering via oxygen manipulation. *Nat. Nanotechnol.* **10,** 333–338 (2015).
41. Zhang, W., Han, W., Jiang, X., Yang, S.-H. & Parkin, S. S. Role of transparency of platinum-ferromagnet interfaces in determining the intrinsic magnitude of the spin Hall effect. *Nat. Phys.* **11,** 496–502 (2015).
42. Pai, C.-F., Ou, Y., Vilela-Leão, L. H., Ralph, D. C. & Buhrman, R. A. Dependence of the efficiency of spin Hall torque on the transparency of Pt/ferromagnetic layer interfaces. *Phys. Rev. B* **92,** 064426 (2015).
43. Jungfleisch, M. B. *et al.* Interface-driven spin-torque ferromagnetic resonance by Rashba coupling at the interface between nonmagnetic materials. *Phys. Rev. B* **93,** 224419 (2016).
44. Ou, Y., Shi, S., Ralph, D. C. & Buhrman, R. A. Strong spin Hall effect in the antiferromagnet PtMn. *Phys. Rev. B* **93,** 220405(R) (2016).
45. Vranken, J., Van Haesendonck, C. & Bruynseraede, Y. Enhanced magnetic surface scattering of weakly localized electrons. *Phys. Rev. B* **37,** 8502–8505 (1988).
46. Gambardella, P. & Miron, I. M. Current-induced spin–orbit torques. *Philos. Trans. A Math. Phys. Eng. Sci.* **369,** 3175–3197 (2011).
47. Sánchez, J. R. *et al.* Spin-to-charge conversion using Rashba coupling at the interface between non-magnetic materials. *Nat. Commun.* **4,** 2944 (2013).
48. Manchon, A. Spin Hall effect versus Rashba torque: a diffusive approach. Preprint at http://lanl.arXiv.org/abs/1204.4869 (2012).
49. Kasap, S. O. *Principles of Electronic Materials and Devices* (McGraw-Hill, 2006).
50. Emori, S. *et al.* Interfacial spin-orbit torque without bulk spin-orbit coupling. *Phys. Rev. B* **93,** 180402(R) (2016).
51. Zhang, S. S.-L., Vignale, G. & Zhang, S. Anisotropic magnetoresistance driven by surface spin-orbit scattering. *Phys. Rev. B* **92,** 024412 (2015).
52. Niimi, Y. *et al.* Experimental verification of comparability between spin-orbit and spin-diffusion lengths. *Phys. Rev. Lett.* **110,** 016805 (2013).
53. Gu, B. *et al.* Surface-assisted spin Hall effect in Au films with Pt impurities. *Phys. Rev. Lett.* **105,** 216401 (2010).
54. Keil, P., Lützenkirchen-Hecht, D. & Frahm, R. Investigation of room temperature oxidation of Cu in air by Yoneda-XAFS. *AIP Conf. Proc.* **882,** 490–492 (2007).
55. Apen, E., Rogers, B. & Sellers, J. A. X-ray photoelectron spectroscopy characterization of the oxidation of electroplated and sputter deposited copper surfaces. *J. Vac. Sci. Technol. A* **16,** 1227–1232 (1998).
56. Platzman, I., Brener, R., Haick, H. & Tannenbaum, R. Oxidation of polycrystalline copper thin films at ambient conditions. *J. Phys. Chem. C* **112,** 1101–1108 (2008).
57. Drobny, V. & Pulfrey, L. Properties of reactively-sputtered copper oxide thin films. *Thin Solid Films* **61,** 89–98 (1979).
58. Demasius, K.-U. *et al.* Enhanced spin-orbit torques by oxygen incorporation in tungsten films. *Nat. Commun.* **7,** 10644 (2016).
59. Nguyen, M.-H., Ralph, D. C. & Buhrman, R. A. Spin torque study of the spin Hall conductivity and spin diffusion length in platinum thin films with varying resistivity. *Phys. Rev. Lett.* **116,** 126601 (2016).

Acknowledgements

This work was supported by PRESTO-JST 'Innovative nano-electronics through interdisciplinary collaboration among material, device and system layers,' JSPS KAKENHI Grant Numbers 26220604, 26103004, 26600078, Spin-RNJ, the Mitsubishi Foundation, the Asahi Glass Foundation, the Mizuho Foundation for the Promotion of Sciences and the Casio Science Promotion Foundation.

Author contributions

H.A., Y. Kageyama and N.E. fabricated devices and collected the data. H.A., Y. Kageyama and Y. Kanno analysed the data. K.A. designed the experiments and developed the explanation. K.A. and H.A. wrote the manuscript. All authors discussed results and reviewed the manuscript.

Additional information

Supplementary Information accompanies this paper at http://www.nature.com/naturecommunications

Competing financial interests: The authors declare no competing financial interests.

Reprints and permission information is available online at http://npg.nature.com/reprintsandpermissions/

How to cite this article: An, H. *et al.* Spin–torque generator engineered by natural oxidation of Cu. *Nat. Commun.* **7**, 13069 doi: 10.1038/ncomms13069 (2016).